CrystEngComm

ROYAL SOCIETY
OF **CHEMISTRY**
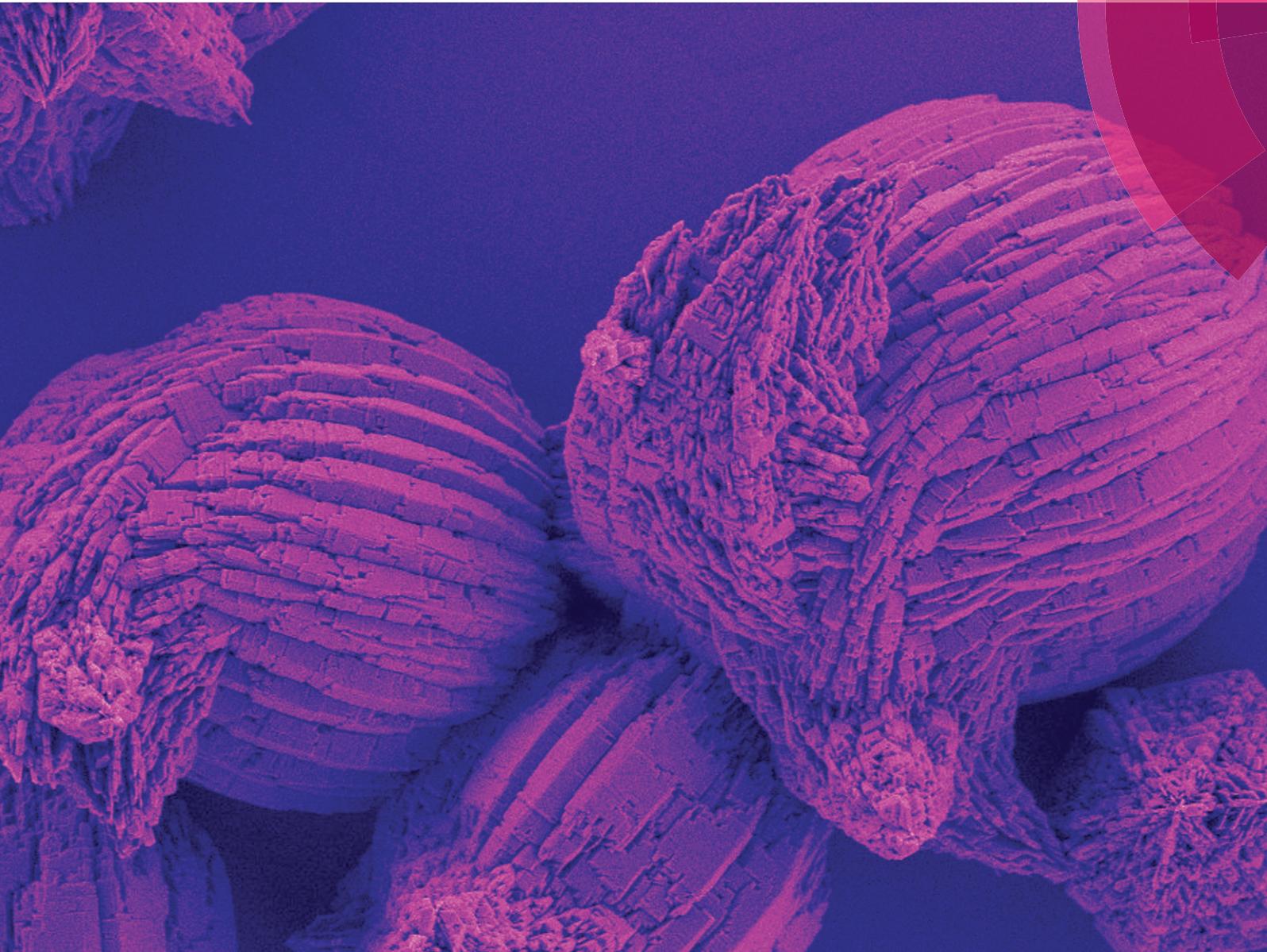
PAPER
Marc-Georg Willinger, Markus Antonietti, Nadine Nassif *et al.*
Structural evolution of aragonite superstructures obtained in the presence
of the siderophore deferoxamine

CrystEngComm

Structural evolution of aragonite superstructures obtained in the presence of the siderophore deferoxamine†

Marc-Georg Willinger,*[a] Julien Polleux,[c] Markus Antonietti,*[c] Helmut Cölfen,[ce] Nicola Pinna[b] and Nadine Nassif*[cd]

The effect of amphoteric siderophore deferoxamine on the crystallization behavior of calcium carbonate was investigated under bioinspired conditions. Amphoteric siderophore deferoxamine possesses self-organization ability, surface activity and ion-chelating properties. It induces in the present case the formation of unusual, highly organized aragonite mesocrystals during the precipitation of calcium carbonate from liquid phase. A detailed investigation of the structure and growth of the particles provides an insight into the role of the deferoxamine and its function in the crystallization process.

Introduction

Biominerals in nature, for example diatoms or coccoliths, inspire researchers to elaborate on the construction of new materials. The mechanisms of biological processes, performed by living organisms to synthesize their inorganic components, are far from being understood, leading researchers to use chemical approaches to mimic them. The motivation is to obtain and understand complex morphologies in simpler model systems. In addition, this field of research is also driven by industrial interest, *e.g.* motivated by the very favourable mechanical properties of biominerals[1] and their application, for instance as organized catalyst supports.[2] Their synthesis in an aqueous environment under ambient conditions from non-toxic, cheap and commonly available compounds is also quite attractive. However, the hierarchical organization found in nature is very difficult to reproduce *in vitro*. Calcium carbonate is one of the most abundant biominerals and, among them, the most studied one due to its scientific and industrial relevance.[3] Calcium carbonate

precipitation represents a relatively complex mineralization process due to the fact that it starts from prenucleation clusters[4] and can proceed *via* liquid or amorphous precursors[5] and finally often involves the coexistence of three stable anhydrous polymorphs: vaterite, aragonite and calcite.[6] Calcite is the thermodynamically stable polymorph under ambient conditions, while aragonite is known to be metastable.[7] The least stable polymorph, vaterite, is the standard kinetic intermediate, but it rapidly recrystallizes to calcite.[8,9]

Especially, aragonite attracts much interest mainly due to its presence in nacre.[10] Nevertheless, the described routes for aragonite synthesis depend on an intricate set-up or well-defined reaction conditions. So far, aragonite was synthesized under high concentration of Mg^{2+} ions,[11,12] with additives such as extracted glycoproteins,[13] which are associated with a β-chitin-silk matrix,[14] and specific imidazolium-based ionic liquids,[15] or under harsh conditions such as elevated temperatures,[16,17] high-power ultrasonic[18] or microwave irradiation.[19] Moreover, aragonite could be synthesized at the air–water interface under compressed monolayers[7,20] *via* an amorphous precursor route,[21] at the liquid–liquid interface in a radial Hele-Shaw cell[22] or by using block copolymer microgels[23,24] where aragonite bundles are obtained. A synthesis in alcoholic medium in the presence of sodium stearate was also proposed to obtain lamellar aragonite.[25]

In this work, a novel model system for complex morpho-synthesis is presented. More specifically, the influence of deferoxamine on the crystallization behavior of calcium carbonate is reported. Deferoxamine belongs to the family of siderophores, a class of low-molecular-weight, iron-coordinating agents produced by plants and microbial organisms. It is clinically used for the treatment of iron overload disease.[26] With its

[a] *Fritz Haber Institute of the Max Planck Society, Department of Inorganic Chemistry, Faradayweg 4–6, 14195 Berlin, Germany. E-mail: willinger@fhi-berlin.mpg.de*
[b] *Humboldt-Universität zu Berlin, Institut für Chemie, Brook-Taylor-Str. 2, 12489 Berlin, Germany*
[c] *Max-Planck Institute of Colloids and Interfaces, Colloid Chemistry, Research Campus Golm, D-14424 Potsdam, Germany. E-mail: nadine.nassif@upmc.fr*
[d] *Laboratoire Chimie de la Matière Condensée de Paris, UMR 7574 CNRS, UPMC, Collège de France, 11 place Marcellin Berthelot, 75231 Paris Cedex 05, France*
[e] *Universität Konstanz, Physikalische Chemie, Universitätsstr. 10, D-78457 Konstanz, Germany*
† Electronic supplementary information (ESI) available. See DOI: 10.1039/c5ce00186b

three hydroxamic acid groups (RCONR′OH) interspaced by two amide groups and terminated with an amine, this biomolecule is a chelating agent[27] with a rich coordination chemistry.[28] Applied to the nonaqueous synthesis of metal oxides, deferoxamine can also provide intra- and intermolecular amide–amide interactions with the potential for supramolecular hybrid nanostructure formation.[29] Our intention to use deferoxamine was to set a model system for a siderophore that is able to bind weakly and reversibly to Ca^{2+} providing high local availability of non-clustered Ca^{2+}, which is an interesting in the frame of natural mineralization processes.

Results

Phase identification and morphology

Identification of the synthesized product was carried out by powder X-ray diffraction (XRD) analysis. The XRD pattern reveals aragonite as the main phase (diffraction peaks 2θ correlated with the (hkl) indices: 26.25 (111), 27.24 (021), 32.79 (121), 33.13 (012), 36.14 (200), 37.28 (031), 37.91 (112), 38.57 (022), 42.96 (122/220), 45.92 (221), 48.44 (202), 50.24 (132), 52.48 (113), 53.02 (023)). Only some weak peaks indicate the presence of calcite as the impurity phase (diffraction peaks 2θ (hkl): 29.44 (104), 39.48 (202), 47.44 (018)). The latter is probably related to uncontrolled growth events, as calcite is the most stable $CaCO_3$ phase, which naturally forms in the absence of any additives. Simulation of the wide-angle X-ray scattering (WAXS) diagram for the aragonite phase using the

Reflex Powder Diffraction module of the MS-Modelling software (Accelrys) including the peak broadening via the Scherrer formalism yielded a primary nanoparticle size of 46 nm. No specific enhancement of planes was observed.

Scanning electron microscopy (SEM) observations of the formed calcium carbonate collected after 24 hours from the bottom of the reaction flasks revealed intricate superstructures of spherical shape as the predominant morphology. In agreement with the XRD results, a few crystals with a rhombohedral morphology were observed (Fig. 1a) as a minority phase. Their morphology is typical for calcium carbonate that precipitates in the absence of additives (Fig. S1†). This suggests that some crystals grow from the continuous phase without being controlled by deferoxamine.

At higher magnification, the SEM images reveal further details of the peculiar crystal superstructure of the obtained particles (Fig. 1b, c and d). Their morphology is characterized by two parts with distinct aspects. The main part is formed by a globular body of 20–50 μm in diameter. It is characterized by striation lines that run from one pole to the other. The other characteristic feature is formed by a bundle of outgrowing structures that generally appear at one of the poles. The length of these outgrowing structures varies from particle to particle but generally reaches a length that is comparable to the diameter of the globular body. Besides a majority of isolated particles, there are some that are connected to each other, either at a common plane or through a complex intergrowth (Fig. 1b, c and S2†).
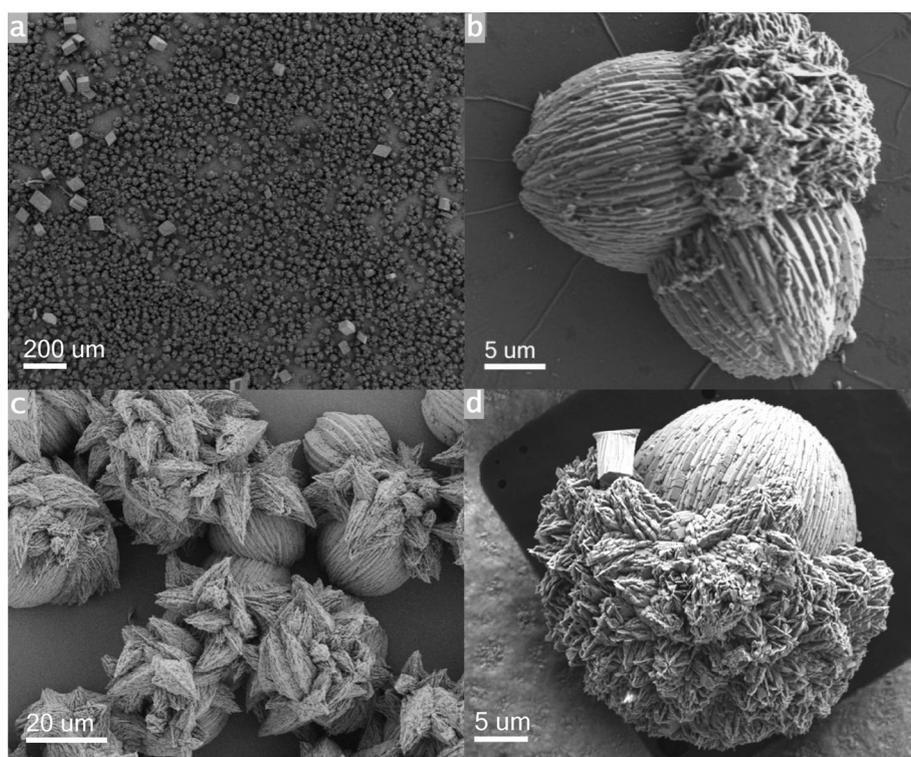

Fig. 1 SEM images of calcium carbonate crystals obtained in the presence of the siderophore deferoxamine (3.2 mg mL^{-1}) showing (a) good homogeneity of the sample at low magnification and (b, c, and d) the predominant, very complex morphology at higher magnification.

It is worth noting that predominant aragonite formation was already observed in previous experiments using poly-tertiary amines.[23,24] Interestingly, precipitation performed with suberohydroxamic acid, made of two hydroxamic acid groups and without amines, does not lead to the formation of unusual crystal morphologies, and instead of spherical aggregates, only the default event of rhombohedral calcite is observed (Fig. S3†). In order to exclude the influence of the counter-anion present in the commercially available deferoxamine in the crystal formation, a control experiment was performed in the presence of methanesulfonic acid. No characteristic changes were observed in the morphology compared to free crystallization, and mainly classical calcite rhombohedra were obtained (few crystals possess a central hole on one face) (Fig. S4†).

Crystal growth

In order to understand the formation mechanism of these highly organized aragonite crystals, samples were investigated by electron microscopy after different times of growth (Fig. 2). After 5 hours, spherical particles with a diameter of about 10 μm were found on the bottom of the reaction flasks. After 9 hours, the particles almost reached their final diameter of about 20–50 μm. They are characterized as a round-like shape that is slightly deformed because of a bulge that forms on one of the poles (Fig. 2a). At higher magnification, a rough, particulate surface morphology is revealed (Fig. 2b). After 13 h of growth, thin lamellas of different lengths can be observed at the surface. They are aligned and give rise to striations that run from one pole to the other (Fig. 2c). At one of the two poles, outgrowth of structures can now be clearly observed. As opposed to the globular body, these outgrowing structures are characterized by lamellas that cross each other at various angles. At higher magnification, small tower-like structures are observed at the sidewalls of an individual lamella (Fig. 2d).

After 24 hours, the rough surface structure of the lamella sidewalls has completely disappeared, and crystallographically flat facets have developed. They show numerous gaps and discontinuities (Fig. 2e and f).

The morphology of the globular body differs from the columnar structures that grow at the poles. Fig. 2g and h show the aspect of these structures in more detail. Each individual outgrowth appears as a stack of thin platelets or pillars that are aligned and oriented towards the tip of the outgrowth. The diameter of each individual outgrowth shrinks through a progressive termination of the outmost crystallites at their growth front. Stepwise, deeper lying platelets are exposed until the axis is reached at the tip of the outgrowth. Looking at the tips of the outgrowing structures from above reveals a well-defined six-fold symmetry (Fig. 2h). Similar pseudo-hexagonal crystals were previously obtained using lithium niobate as a carbonate free single-crystal substrate. In that case, epitaxial aragonite growth occurred through the arrangement of cations on the substrate.[30]
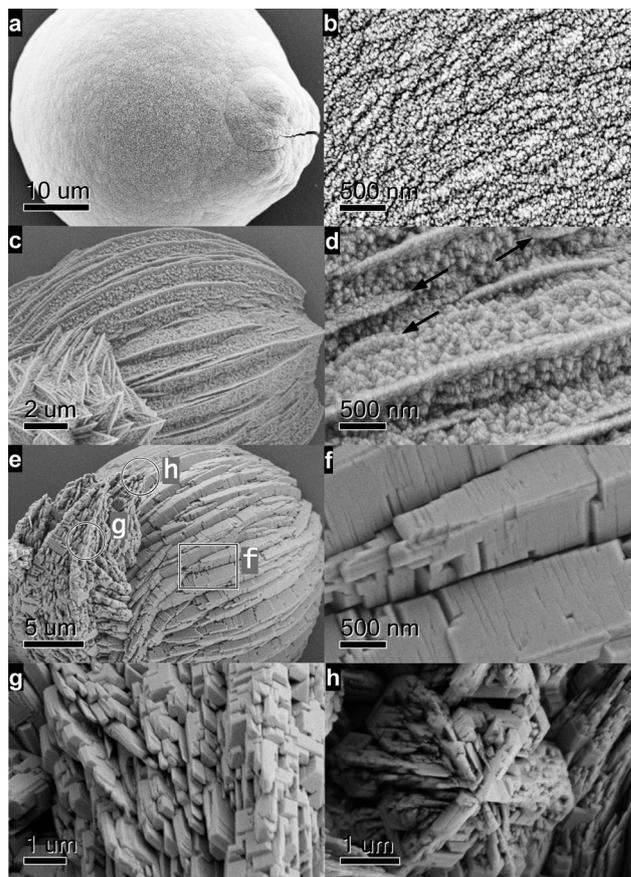

Fig. 2 Overview (left) and high magnification SEM images (right) recorded from particles at different growth stages show the progressive development of the complex morphology. a) and b) were recorded after 9 h; c) and d) after 13 h; and e) and f) after 24 hours of growth, respectively. g) and h) show details of the characteristic outgrowth and the apex of an outgrowth viewed from the top, respectively, revealing a hexagonal assembly of platelets.

Aragonite–siderophore interactions

In order to investigate the role of the siderophore deferoxamine in the formation of the aragonite structures, dynamic light scattering (DLS) investigations were performed on two $CaCl_2$/deferoxamine solutions with molar ratios of 1:1 and 2:1, which were previously gently sonicated. DLS analysis of both primary $CaCl_2$/deferoxamine solutions indicates deferoxamine-Ca aggregates of about 0.5–2.7 nm, with an average hydrodynamic radius of ~1 nm, but no other species. This supports our point of view that siderophores essentially improve the availability of single Ca^{2+} ions or very small clusters, but not bigger clusters or colloids. An excess of $CaCl_2$ favors calcite crystallization, as seen by the higher number of rhombohedral particles that formed in its presence with a molar ratio of 2:1 (Fig. 1a) in comparison to a ratio of 1:1. This observation is further supported by previous studies,[31] which showed that deferoxamine only allows the monochelation of calcium(II). Interestingly, the monochelation of calcium(II) with deferoxamine has a low stability constant due to the large radius of the cation, which is nearly twice as large as

that of iron, and the spacers that bridge the three hydroxamic acid groups are comparably short.[31] The defined small aggregates could only be detected after weak sonication of the CaCl$_2$/siderophore solution, suggesting that the siderophore needs some activation to be dissolved homogeneously and interact with Ca^{2+} since it is stabilized by the potentially by hydrogen bridges between single deferoxamine entities. Crystallization events simply become more homogeneous when the starting conditions are more defined. Although interactions between calcium(II) and deferoxamine are expected to be very weak until reaching a pH of around 7, an effect on the crystal growth could be observed already at pH 5.8 in our study. Starting from this pH, the presence of the siderophore increases the concentration of calcium in the solution, due to the binding equilibrium.

The primary crystal seed is known to play a very important role in the determination of whether calcite or aragonite forms, and the polymorph can even be encoded in an amorphous CaCO$_3$ precursor phase.[32] Indeed, our data shows that once the growth of a calcite particle is initiated, it would just keep on growing while ignoring the presence of the siderophore. It is probable that siderophore molecules interact differently with the growing structures in a time-dependent manner. Indeed, the total charge of deferoxamine at different pH values may define its binding properties and thus control the mode of aragonite growth. During the mineralization protocol, ammonia and CO$_2$ diffuse into the CaCl$_2$ solution, leading to an increase in pH from 5.8 to 9.5 throughout the crystallization process. With dissociation constants equal to pH 8.30, 9.00, 9.46 and 10.4 that correspond to that of the three hydroxamic acids and the amine group, respectively,[31] deferoxamine is positively charged at pH 5.8 and may electrostatically bind to hydrogen carbonate (HCO$_3^-$) via the ammonium group but not to calcium(II) at the beginning of the crystallization process. During the increase in pH, although the total charge of deferoxamine becomes neutral and then negative, the monochelation of calcium(II) to this siderophore remains rather weak, as the stability constant of the complex is not significantly changed.[31]

In spite of the rather high deferoxamine concentrations, it may come as a surprise that the organic content of the final structures is very low, as determined by TGA. This just means

that the siderophore is only active as a growth modifier, but is effectively released at the final pH and within the final structure. This low consumption makes such a modifier also useful for technical mineralization recipes.

Crystallographic investigation of the aggregates

A more detailed insight into the early stages of the structural evolution was obtained by crushing the samples and sampling some of the obtained fractions. The SEM image in Fig. 3a shows a random agglomeration of nanoparticles that was abstracted from a fully-grown structure. The TEM image of a slightly more ordered structure that was abstracted from a sample after 9 h of growth is shown in Fig. 3b. It reveals nanoparticles that are assembled in a branched, dendritic-like manner. As indicated by the distribution of the (111) spots in the corresponding electron diffraction pattern, the nanoparticles however show a comparably high crystallographic alignment with only some minor distortions, i.e. they obviously grow and arrange via "vectorial alignment". Similar structures, although slightly denser and with clearly developed pillar-like structures, were also observed in the fragments of fully-grown particles (Fig. 3c).

Putting the crushed pieces in the context of complete particles was, however, quite challenging and could only be achieved by analysing distorted growth events. Some of the particles that nucleated at the wall of the reaction flask grew such that the glass cut a plane through their center. Particles "cut" in this manner reveal their inner structure and allow the study of changes in the growth modes from the center to the surface. In Fig. 4, two particles are shown revealing their equatorial and longitudinal inner structures, respectively.

Interestingly, in both cases, the shape of the final particle seems to be unaffected by the presence of the glass substrate on which they grew. Indeed, the usual morphology is obtained, such as if the particles were cut after growth. The presence of both longitudinally and equatorially cut particles at the glass surface could be a hint on the role that the inner, central region of the particles plays in defining the growth directions and crystallographic arrangement of crystalline domains of the complex shape and thus the final shape. In the very center, the nanoparticle aggregate does not show any
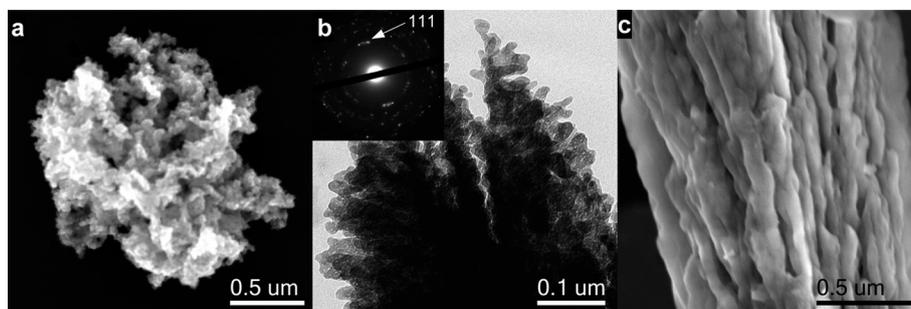

Fig. 3 SEM images recorded from fractions obtained by crushing particles after 24 h of growth are shown in a) and c). In b), a TEM image of a fraction obtained by crushing a particle after 9 h of growth is shown. The corresponding diffraction pattern is shown in the inset.
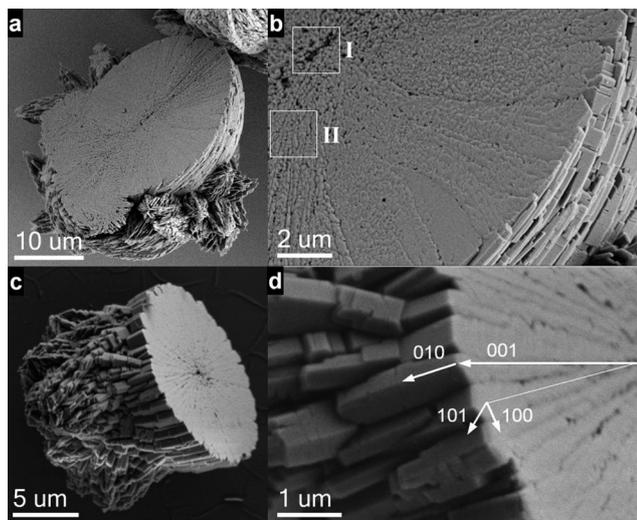
Fig. 4 SEM images recorded form two particles in which the nucleation at the wall of the flask led to a longitudinal and equatorial cut, respectively. Crystallographic directions are indicated in d).

signs of pre-determined directionality or anisotropy. From the center to the outside, the structural density gradually increases and orientation relationships emerge. This is clearly shown in Fig. 4b. The aspect of the central region, marked as square I in Fig. 4b, is similar to that of the agglomeration shown in Fig. 3a. Further away from the center, in the region marked as square II, a pillar-like, dendritic structure, similar to that in Fig. 3c, can be identified. Hence, the crushed samples shown in Fig. 3 are indeed from the inner volume and resemble the first growth stages of the particles. Formation of the particles therefore starts with a loose agglomeration of nanoparticles at the center. It is followed by the formation of nanoparticulate, dendritic structures that radiate outwards. This is the region where first signs of local crystallographic alignment can be observed (Fig. 3b), presumably following the so-called oriented attachment. It can finally result in the formation of a so-called mesocrystal, which however cannot be proven in the present case.[33]

As ordinary aragonite nanoparticles hardly show oriented attachment, we assume that the nanoparticles observed at

this growth stage are still stabilized by the siderophore, locally liberated throughout the consumption of Ca^{2+} by the precipitating nanoparticles. Nucleation and attachment of further nanoparticles lead to further densification and formation of extended crystallographic coherent domains and the formation of sheet-like crystals growing radially in the [001] direction. A possible underlying concept for the orientation alignment is crystal growth competition,[34,35] according to which particles with a fast growing direction (here, the [001]) pointing towards the growth front successfully compete and dominate over differently oriented particles. The principle is schematically illustrated in Fig. 5. Once the fast growing direction is determined, the local alignment of the remaining crystallographic axes follows under the constraint of confined space. The radial symmetry is then a product of all the crystal slices growing radially outwards in the [001] direction. With increasing density and probably also with a change in the pH and a drop in Ca concentration, the growth mode changes.

Surface energy minimization then results in the formation of joint, extended crystallographic facets terminating the superstructure. The transformation of the rough surface observed at an earlier growth stage into flat crystallographic facets can carefully be followed by comparing Fig. 2d with f.

Observation of the striation lines at the surface of the globular body by high resolution SEM (Fig. 6a) reveals numerous growth discontinuities and a nanoscale surface texture, being the memory of the primary nanoparticulate building blocks. However, the densely packed domains terminate with common planes, similar to what is expected for the case of a single crystal. Indeed, the single crystal-like behaviour is confirmed by high resolution TEM imaging. The image shown in Fig. 6b reveals continuous lattice fringes and an agreement in crystallographic orientation even across gaps. Thus, the behaviour is very similar to the case of nacre, in which the individual aragonite platelets diffract like single crystals although they are made up of densely packed nanocrystalline units.[36]

Another interesting point to note here is the presence of an amorphous surface layer, similar to what was described by Nassif *et al.* for the case of nacre[37] and synthetic aragonite.[23]
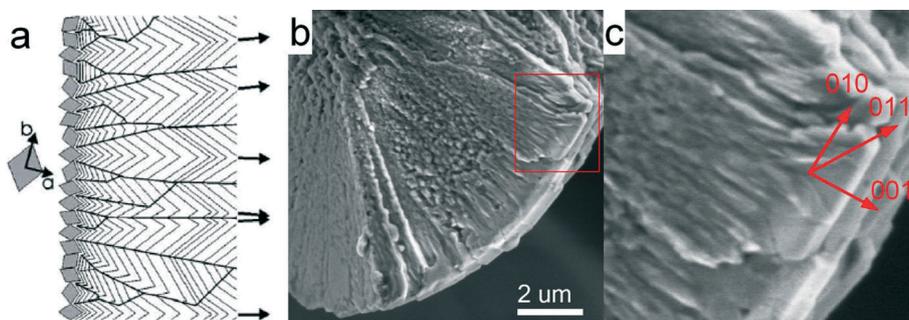

Fig. 5 Growth competition gradually leads to the evolution of a common growth direction. a) shows a scheme of the principle, taken from , while b) and c) show the transition from randomly attached particles in the center to well developed crystalline facets on the surface of the particles.
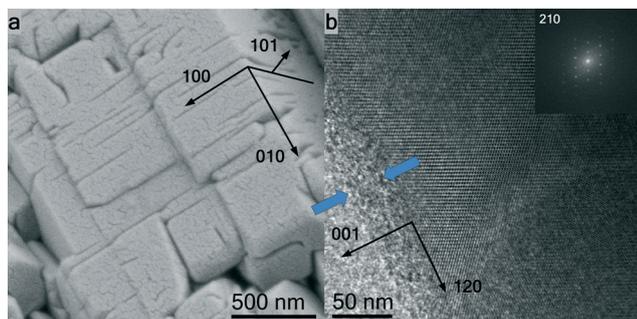
Fig. 6 a) High resolution SEM image recorded from the surface of a particle, showing that the striation lines are in fact made up of densely packed nanocrystalline units. The high-resolution image shown in b) was recorded from the edge of the globular body, in a region similar to what is shown in a). Lattice fringes and corresponding power spectrum reveal a single crystal-like behaviour. The presence of an amorphous surface layer is pointed out by arrows.

The current, repeated observation indicates that the amorphous surface layer is a natural feature of aragonite crystals grown from water in the equilibrium state.

For a deeper understanding of the growth of the particles and their final shape, the relationship of the crystal orientation of aragonite to the particulate morphology has to be revealed.

In order to do so, detailed HRTEM imaging was performed along the surface of the globular body of individual particles. The combination of SEM and TEM and observations over a large range of magnifications was crucial for relating information obtained on the atomic scale to the overall structural motif. The SEM overview image and the corresponding TEM images are shown in Fig. 7. The HRTEM investigations and the analysis of lattice fringes conclusively revealed that the particles indeed grow radially along the *c* axis of aragonite. The striation lines running in the longitudinal direction from one of the poles to the other coincide with the crystalline *b* axis. Consequently, the remaining *a* direction runs around the globe in a plane parallel to the
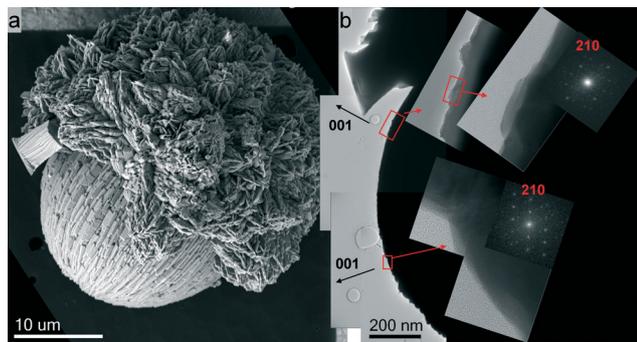
equator. Crystallographic orientations are indicated by arrows in Fig. 5c, 6a, b, and 7b.

Formation of the well-structured outgrowth

Similar to the case of the globular body, orientational relationships in the outgrowing structures have been revealed by observing uncrushed particles over a large range of magnifications by SEM and TEM. As shown in Fig. 8, the axis of the outgrowth follows the crystallographic *c* axis. This is in accordance with the direction of maximal growth controlling the main body of the particle. It is interesting, though, that the structural aspect of the outgrowth is very different from that of the globular body. The TEM investigations demonstrate that the stacked platelets forming the outgrowth are crystallographically related to one another. Indeed, as shown in Fig. 8d, the lattice fringes of stacked platelets are in perfect agreement and, besides the change in thickness, cannot be distinguished from a single crystal. The crystallographic relation of all the stacked platelets is also manifested in the six-fold symmetry of the resulting mesocrystal, which can be observed when the outgrowth is viewed along the polar axis (Fig. 2h). Similar to the surface of the globular body, the stacked platelets show an amorphous surface layer.
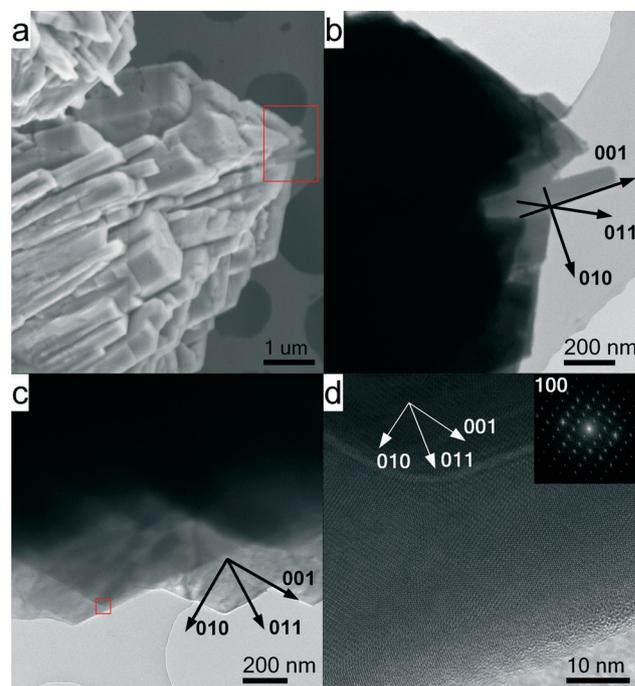

Fig. 8 a) and b) show SEM and TEM images, respectively, recorded from the same tip of one outgrowth. Growth directions and terminating facets are indicated. c) and d) show the overview and high resolution image of stacked platelets forming up the outgrowth, respectively. The red square indicates the region from where the high resolution image in d) was recorded. Inset in d) shows the corresponding fast-Fourier transformation. The arrangement of spots is in agreement with the one expected for the (100) zone axis of aragonite. Furthermore, the spot pattern reveals perfect crystallographic matching between the imaged platelets.

Fig. 7 SEM (left) and TEM (right) composition (acquired on the same particle) demonstrating how the growth directions of the globular body were determined. Two regions, from which high-resolution images were recorded, are shown with the corresponding power spectra in the insets.

Once the crystallographic relationships have been revealed, the initial reason for the formation of the outgrowth has to be elaborated. On a sphere, radial growth with an alignment of the crystallographic axis faces some constraints (similar to the "hairy ball theorem"[38]).

It has already been shown by SEM images recorded at an early growth stage (Fig. 2) that the same lamellas that give rise to the striations at the surface of the globular body are also found at the outgrowth. However, while they are running parallel to the equatorial belt, with their *b* axis pointing to the longitudinal direction, they are crossing each other at the pole, as indicated in Fig. 9. Aragonite is known to form polycyclic twins at the (110) planes. These conditions are met when [010] or [100] directions cross at 120°. Indeed, outgrowing structures are formed specifically at positions where lamellae cross at 120°. Under such conditions, a twin is formed. This is a straightforward explanation for the six-fold symmetry that is revealed when the outgrowing structures are viewed from the top as shown in Fig. 2h and 9c.

Therefore, the outgrowing structures are formed as a consequence of the radial growth and crystallographic alignment combined with the ability of aragonite to form twins. As shown in Fig. 4a, one can see that the outgrowth on the left shows its roots deep inside the particle. The first signs of the formation of outgrowing structures are therefore manifested in a relatively early growth stage (*i.e.*, after less than 9 h, Fig. 2a). The corresponding region, which is characterized by *intergrowth* and twinning, expands faster due to an increased growth speed and hence requires more space. Presumably, the attachment of the growth carrying nanoparticles adds up at the point where lamellae intercept in a preferred angle and where a cyclic twin is formed. This is possibly due to a combination of rather good stabilization of the nanoparticles by the siderophore and field effects which allow the particles in later stages of reaction to discriminate between different positions of aggregation, thus preferring twinning positions where the fields are not compensated.

A strong indication of the presence of field effects is found in view of the fact that the outgrowth is exclusively formed on only one of the poles. As seen in Fig. 5c, aragonite grows preferably along [001], which is the fast growth direction. The {001} faces are, however, highly polar faces and not stabilized by the siderophore. Consequently, the surfaces on the globular body are mainly defined by (101) and some (100) planes (see Fig. 4d). However, the faces of outgrowing structures at the pole mainly constitute (100) planes, defining the thin direction of the aragonite slices (thereby greatly stabilizing and also loosing against [001] in the growth competition). The pole-to-pole direction of the striation lines is in the [010] direction, associated with polar surfaces. As the siderophore binds to carbonate especially at the more acidic pH at the beginning of the crystallization reaction but not or only weakly to calcium ions,[31] one of the (010) faces of the primary nanoparticles, the negative side, is hindered in growth causing a dipole field along [010]. If we define the equatorial cut through the superstructure to be along the [100] direction, this gives an exact cycle, *i.e.* all [100] directions sum up into the same circular direction. The (010) cut is more of an ellipse, and the structure must be twinned (as all the [100] directions are aligned already). Indeed, the "cut through the particle" reveals this pole-to-pole distortion by its lower structural density (see Fig. 4a) along the pole-to-pole axis. This means that all meridians are oriented in the same direction, supported by twinning structures along the axis. By superstructure formation, this sums up to the discussed fields at the poles where the "negative pole" does not outgrow, while the "positive pole" attracts further nanoparticles and leads to the found pronounced structured outgrowth. Such inner field effects were found for $CaCO_3$ before and can lead to very specific superstructures of remarkable beauty.[39,40] The fact that the siderophore, contrary to the previously reported cases, binds here, mostly to the (100) and (010) faces of aragonite (instead of the (001) of calcite), is attributed to appropriate charge distances in the surface and ligand and pattern recognition.

Conclusion

This study shows the formation of aragonite superstructures through a non-classical crystallization process. In contrast to the well-organized natural aragonite crystals that are intimately associated with an organic matrix in mollusk shells, the crystal superstructure here is achieved only with the use of a soluble small molecule. Nevertheless, the siderophore as an amphoteric additive with time/pH-dependent interaction with the crystals is close to the soluble part of natural biomineralization proteins, which are also amphoteric. We identified its action in an at least threefold fashion: stabilizing nanoparticles, controlling their alignment by stabilization of specific crystal faces, and controlling a complex dynamic self-organization process which finally results in a delicate crystal superstructure where primary crystals are oriented along
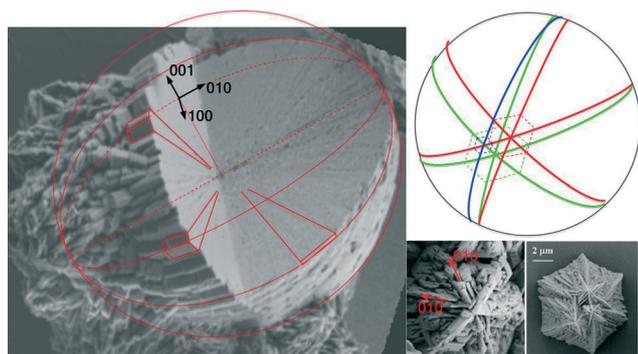

Fig. 9 The image on the left side shows a montage made from the half spheres shown in Fig. 4a and c. Crystallographic directions as well as crystalline domains and striation lines are indicated. Aragonite grows radially from the center, with the *c* axis pointing outwards and the *b* axis pointing longitudinally towards the poles. Hence, crystalline domains are oriented parallel to the equatorial belt, but crossing each other in the region close to the poles, as schematically shown in the diagram on the right side. Small pictures show that polycyclic twinning occurs at the poles.

the radial growth axis, along the equator or latitudes, and along the meridians in three well-defined fashions. Hence, great complexity can be achieved by synergy between pH-dependent polymer/crystal interaction and crystallization. This process, which should be adaptable to other systems, may help to better understand the presence of additives and especially small molecules that could influence the kinetics of crystal growth as well as provide an interesting aspect of aragonite crystal growth in natural media.

Experimental procedure

Synthesis

Calcium carbonate polycrystals were grown by diffusion of carbon dioxide into calcium chloride solutions according to the gas diffusion method[34] by thermal decomposition of ammonium carbonate. Experiments were performed at room temperature ($22 \pm 1^\circ C$). Two flasks containing 0.01 M calcium chloride solution (20 mL) mixed with different concentrations of deferoxamine mesylate salt powder from Sigma-Aldrich (3.2 and 6.4 mg mL^{-1}; MW = 656.79 g mol^{-1}, *i.e.* corresponding to molar ratios of 2:1 and 1:1 calcium to deferoxamine, respectively) and fresh ammonium carbonate (2 g) were placed into a closed chamber (1000 cm^3). The aqueous solutions of siderophore deferoxamine/$CaCl_2$ were prepared in doubly distilled water, sonicated for 10–15 minutes and bubbled with N_2 overnight before use. The decomposition of ammonium carbonate produced ammonia and carbon dioxide diffusing through 5 needle holes pierced into the parafilm cover of the flasks. The initial solution was slightly acidic (pH 5.8) but the pH value rose to 9.5 because of the dissolved NH_3. After different ageing times (5, 9, 13 and 24 hours), the sample was removed from the solution, rinsed with filtered water and acetone, and then air-dried.

Crystal characterization

The crystals were washed with distilled water then ethanol and dried in air for further characterization. Powder X-ray diffraction (XRD) patterns were recorded on a PDS 120 diffractometer (Nonius GmbH, Solingen) with Cu-K$_\alpha$ radiation. The SEM measurements were performed using a LEO 1550 – GEMINI with gold-coated samples. FT-IR spectra were recorded either with a Nicolet Impact 400 or a BioRad FTS6000 spectrometer.

Electron microscopy investigations have been performed at the Department of Ceramics and Glass Engineering at the University of Aveiro, Portugal, using a JEOL 2200FS transmission electron microscope and a Hitachi SU70 scanning electron microscope.

Dynamic light scattering (DLS) experiments were performed using a Malvern Nano ZS90 equipped with a HeNe laser (λ = 632.8 nm) and a power of 10 mW. The scattered light was collected at an angle of 90°. A polystyrene curve was used for each measurement and filled with 3 mL of the freshly prepared deposition solution through a 0.02 μm size filter. The time t = 0 is defined as the introduction of the sample in the apparatus. The temperature of this equipment is maintained by a Peltier element. A reaction temperature of 20 °C was reached after about 3 min. Correlation functions were recovered every 150 s for a total duration of about 90 min. Data evaluation was performed with the software supplied by the manufacturer employing the analysis mode for the multimodal sample, which yields an average value for the hydrodynamic radius and the polydispersity index, which are characteristics of the particle size distribution. DLS measurements were triplicated for each sample to ensure the reproducibility under the preparation conditions.

References

1 H. Nakahara, *Calcification of Gastropod Nacre Biomineralization and Biological Metal Accumulation*, ed. P. Westbroeck and E.W. De Jong, D. Reidel Publishing Co., Dordrecht, 1983, 225230.

2 D. Green, D. Walsh, S. Mann and R. O. C. Oreffo, *Bone*, 2002, **30**, 810–815.

3 H. Cölfen, *Curr. Opin. Colloid Interface Sci.*, 2003, **8**, 23; F. C. Meldrum , *Int. Mater. Rev.*, 2003, **48**(3), 187–224.

4 D. Gebauer, A. Voelkel and H. Coelfen, *Science*, 2008, **322**(5909), 1819–1822.

5 D. Gebauer, M. Kellermeier, J. D. Gale, L. Bergstroem and H. Coelfen, *Chem. Soc. Rev.*, 2014, **43**, 2348.

6 K. M. McGrath, *Adv. Mater.*, 2001, **13**, 989.

7 A. L. Litvin, S. Valiyaveettil, D. L. Kaplan and S. Mann, *Adv. Mater.*, 1997, **9**, 124.

8 F. Lippman, in *Sedimentary Carbonate Minerals*, ed. W. von Engelhardt, T. Hahn, R. Roy and P. J. Wyllie, Springer, Berlin, 1973.

9 W. D. Carlson, in *Reviews in Mineralogy, Vol. 11*, ed. R. J. Reeder, Mineralogical Society of America, Blacksburg, 1983, p. 191.

10 H. A. Lowenstam and S. Weiner, *On Biomineralization*, Oxford University Press, New York, 1989.

11 I. Lee, S. W. Han, H. J. Choi and K. Kim, *Adv. Mater.*, 2001, **13**, 1617.

12 A. Sugawara and T. Kato, *Chem. Commun.*, 2000, 487.

13 A. M. Belcher, X. H. Wu, R. J. Christensen, P. K. Hansma, G. D. Stucky and D. E. Morse, *Nature*, 1996, **381**, 56.

14 G. Falini, S. Albeck, S. Weiner and L. Addadi, *Science*, 1996, **271**, 67.

15 Y. Zhao, Z. Chen, H. Wang and J. Wang, *Cryst. Growth Des.*, 2009, **9**(11), 4984–4986.

16 J. Kuther, G. Nelles, R. Seshadri, M. Schaub, H. J. Butt and W. Tremel, *Chem. – Eur. J.*, 1998, **4**, 1834.

17 Y. Ota, S. Inui, T. Iwashita, T. Kasuga and Y. Abe, *J. Am. Ceram. Soc.*, 1995, **78**, 1983.

18 G.-T. Zhou, J. C. Yu, X-C. Wang and L-Z. Zhang, *New J. Chem.*, 2004, **28**, 1027.

19 A. Rizzuti and C. Leonelli, *Powder Technol.*, 2008, **186**, 255–262.

20 B. R. Heywood and S. Mann, *Chem. Mater.*, 1994, **6**, 311.

21 F. F. Amos, D. M. Sharbaugh, D. R. Talham, L. B. Gower, M. Fricke and D. Volkmer, *Langmuir*, 2007, **23**, 1988–1994.

22 D. Rautaray, A. Banpurkar, S. R. Sainkar, A. V. Limaye, N. R. Pavaskar, S. B. Ogale and M. Sastry, *Adv. Mater.*, 2003, **15**, 1273.

23 N. Nassif, N. Gehrke, N. Pinna, N. Shirshova, K. Tauer, M. Antonietti and H. Cölfen, *Angew. Chem.*, 2005, **117**, 6158.

24 K. Tauer and V. Khrenov, *et al.*, *Macromol. Symp.*, 2005, **226**, 187–201.

25 C. Wang, Y. Xu, Y. Liu and J. Li, *Mater. Sci. Eng., C*, 2009, **29**, 843–846.

26 T. B. Chaston and D. R. Richardson, *Am. J. Hematol.*, 2003, **73**, 200.

27 C. J. Marmion, D. Griffith and K. B. Nolan, *Eur. J. Inorg. Chem.*, 2004, **15**, 3003.

28 B. Kurzak, H. Kozowski and E. Farkas, *Coord. Chem. Rev.*, 1992, **114**, 169.

29 J. Polleux, N. Pinna, M. Antonietti and M. Niederberger, *J. Am. Chem. Soc.*, 2005, **127**, 15595–15601.

30 B. Pokroy and E. Zolotoyabko, *Chem. Commun.*, 2005, 2140.

31 E. Farkas, É. A. Enyedy and H. Csóka, *Polyhedron*, 1999, **18**, 2391.

32 J. H. E. Cartwright, A. G. Checa, J. D. Gale, D. Gebauer and C. I. Sainz-Díaz, *Angew. Chem., Int. Ed.*, 2012, **51**, 11960–11970.

33 M. Niederberger and H. Coelfen, *Phys. Chem. Chem. Phys.*, 2006, **8**, 3271–3287.

34 D. J. Barnes, *Science*, 1970, **170**, 1305–1308.

35 A. G. Checa, T. Okamoto and J. Ramírez, *Proc. R. Soc. B*, 2006, **273**, 1329–1337.

36 M. Rousseau and E. Lopez, *et al.*, *Biomaterials*, 2005, **26**, 6254–6262.

37 N. Nassif, N. Pinna, N. Gehrke, M. Antonietti and H. Cölfen, *Proc. Natl. Acad. Sci. U. S. A.*, 2005, **102**, 12653–12655.

38 http://en.wikipedia.org/wiki/Hairy_ball_theorem.

39 L. Addadi, J. Moradian, E. Shay, N. G. Maroudas and S. Weiner, *Proc. Natl. Acad. Sci. U. S. A.*, 1987, **84**, 2732.

40 T. Wang, M. Antonietti and H. Colfen, *Chem. – Eur. J.*, 2006, **12**(22), 5722–5730.